J. Fluid Mech. (2009), *vol.* 637, *pp.* 443–473.
doi:10.1017/S002211200999070X

Numerical simulation of viscous, nonlinear and progressive water waves

ASHISH RAVAL[1]†, XIANYUN WEN[1,2] AND MICHAEL H. SMITH[1]

[1]Institute for Climate and Atmospheric Science, School of Earth and Environment, University of Leeds, Leeds LS2 9JT, UK

[2]The Centre for Computational Fluid Dynamics, University of Leeds, Leeds LS2 9JT, UK

(Received 15 October 2008; revised 3 June 2009; accepted 3 June 2009; first published online 23 September 2009)

A numerical simulation is performed to study the velocity, streamlines, vorticity and shear stress distributions in viscous water waves with different wave steepness in intermediate and deep water depth when the average wind velocity is zero. The numerical results present evidence of 'clockwise' and 'anticlockwise' rotation of the fluid at the trough and crest of the water waves. These results show thicker vorticity layers near the surface of water wave than that predicted by the theories of inviscid rotational flow and the low Reynolds number viscous flow. Moreover, the magnitude of vorticity near the free surface is much larger than that predicted by these theories. The analysis of the shear stress under water waves show a thick shear layer near the water surface where large shear stress exists. Negative and positive shear stresses are observed near the surface below the crest and trough of the waves, while the maximum positive shear stress is inside the water and below the crest of the water wave. Comparison of wave energy decay rate in intermediate depth and deep water waves with laboratory and theoretical results are also presented.

1. Introduction

Free surface flows are important in many areas of engineering and applied science, including mechanical and chemical engineering, naval hydrodynamics, physical oceanography, air–sea interaction, marine boundary layer flows, capillary and porous media flows. In naval hydrodynamics, interaction of wakes and vortices with the free surface is of particular interest as revealed by synthetic-aperture-radar (SAR) imaging. Tsai & Yue (1996) outlined many aspects of the computation of the nonlinear free surface flows and water waves is one such application area. As global and ocean circulation models are developed and advanced to a stage to include the coupled air–sea interaction, it becomes increasingly important to study the near surface physical processes which can affect energy, momentum, heat and mass exchange on the water surface. Moreover, correct understanding and better accuracy are highly desirable while studying breaking waves and the resulting heat, mass and gas transfer as well as their interactions with each other.

† Email address for correspondence: a.raval@gmail.com

Water waves are generally studied under three broad categories: (*a*) potential flow, (*b*) inviscid rotational flow and (*c*) viscous flow. The main characteristics of the potential flow are inviscid, irrotational velocity field and exclusion of turbulence. In a potential flow, the continuity and momentum equations for the flow are replaced by the Laplace equation for the velocity potential. The analytical solution can be found under corresponding kinematic, dynamic, lateral and bottom boundary conditions. This is well documented in Lamb (1932) and Milne-Thomson (1994) and is also elaborately explained in Dean & Dalrymple (1984). Moreover, research on this subject spans many years and is covered widely in many books and journals.

A major hurdle to the above potential flow assumption is that it does not include all the characteristics of the flow. Hence, it is inaccurate for the flows with a boundary layer, which includes water waves. According to Saffman (1981), if vorticity $\omega = 0$ everywhere in an incompressible fluid, the fluid in reality ceases to be a fluid; it loses its infinite number of degrees of freedom, which makes possible the infinite variety of fluid motion. In the past, there had been several attempts to formulate vorticity in the inviscid solution for water waves. An analytical solution is outlined in Lamb (1932) for inviscid water waves with vorticity, as given by the exact solution of Gerstner's trochoidal wave theory (Gerstner 1802). Vanden-Broeck (1996) used a boundary integral equation method to numerically compute the periodic waves with constant vorticity. Teles da Silva & Peregrine (1988) used a boundary integral method for periodic and solitary waves with constant vorticity. However, these results are limited in application due to special vorticity distribution. Dalrymple & Kirby (1986) used boundary integral method to study the interaction of small amplitude water waves with bottom ripples. More recently, Constantin (2001) and Constantin, Sattinger & Strauss (2006) have tried to formulate the solution for the inviscid and rotational water waves. For a viscous low-Reynolds-number flow, the convection terms in the full Navier–Stokes equations are dropped and original nonlinear equations become linear. This allows an analytical solution to be found for the water wave with small amplitude. The solution for low-Reynolds-number viscous water waves is outlined in Kinsman (1965) and Lamb (1932). Behroozi (2004) used the principle of conservation of energy to derive the relationship between fluid viscosity and decay coefficient of the surface waves. Wang & Joseph (2006) used viscous potential flow and viscous correction potential flow method to analyse the decay of free gravity wave due to viscosity. In recent years, in order to include the effect of viscosity, a visco-potential free surface flow formulation has been developed by Dutykh & Dias (2007) and Liu & Orfila (2004).

Several numerical methods have been developed for free surface flows. They include front tracking method by Tryggvason *et al.* (2001), the boundary integral method by Hou, Lowengrub & Shelley (2001), the phase field method by Jacqmin (1999), the second gradient method from Jamet *et al.* (2001), level set method by Sethian (1999) and marker-and-cell method (MAC) by Harlow & Welch (1965). Smoothed particle hydrodynamics (SPH) method is relatively new development; several works pertaining its applications in free surface flows are outlined by Monaghan (1994), Monaghan & Kos (1999) and Dalrymple & Rogers (2005). By imposing the condition of zero shear stress on water surface, Huang, Zhang & Lee (1988) and Dong & Huang (2005) used the finite analytic method from Chen & Chen (1982, 1984) and a modified MAC method to produce the velocity distributions and energy decay rate of viscous water waves when they investigated the generation and propagation of water waves in a viscous wave plume. Similarly, using the kinematic boundary condition on the water surface, Thomas, Leslie & Williams (1995), Liu & Lin (1997), Li & Fleming (2001),

Park *et al.* (2003), Maronnier, Picasso & Rappaz (2003), Hur & Mizutani (2003), Chen & Nokes (2005) and Lin (2008) calculated the location of water surface by specifying either zero stress or zero pressure or total zero shear stress on water surface. All of these calculations have included only water and the air is excluded from consideration. Hirt & Nichols (1981) developed a volume of fluid (VOF) method to calculate the shape of free surface, a comprehensive review of the VOF was given by Scardovelli & Zaleski (1999). Zwart, Burns & Galpin (2007) have developed a VOF method by defining the volume fractions of air and water separately and used a high resolution scheme for the equations of mass conservation of air and water, all equations for velocity, pressure and volume fractions of fluids are then solved simultaneously in a coupled system. Unlike the VOF method developed by Hirt & Nichols (1981) and other methods such as MAC, SPH and height function methods, this method not only includes both water and air retaining the continuity of velocity, pressure and shear stress on water surface but also eliminates the need to reconstruct the shape of water surface during the calculation. Current work uses this method to simulate the progressive water waves.

By their nature water waves are transient, nonlinear, rotational and viscous. However, since these properties make them complex and difficult to analyse, they are often simplified to linear, irrotational and inviscid water waves. By doing so, many important features related to understanding of basic physics in the viscous water waves have not been revealed. The vorticity and shear stress are two such important quantities in wave dynamics which need thorough examination. The presence of vorticity and shear stress is a strong indication of rotational and viscous behaviour of the water waves. In the past, most of the work related to the vorticity in the water waves has been confined to the spilling breaker flows, as outlined by Duncan *et al.* (1994), Lin & Rockwell (1995) and Dabiri & Gharib (1997). Lundgren & Koumoutsakos (1999) have described free surface viscous flows in a vortex dynamics formulation using vorticity field as the primary variable and expressing velocity as a functional of the vorticity through the Biot–Savart integral thus eliminating pressure from the formulation. However, the zero shear stress boundary condition used to calculate the value of the vorticity on the surface is not applicable in the cases where wind is blowing over the moving water waves. According to Longuet-Higgins (1992), the occurrence of 'parasitic capillaries' on the forward face of moderately short gravity waves is the major source of vorticity. Fulgosi *et al.* (2003) performed direct numerical simulation (DNS) of the turbulence in a shear air–water flow with a deformable interface in a capillary wave regime. According to Thais & Magnaudet (1995), there are indications of the existence of an orbital vorticity below waves when wind is present. Even weak, this vorticity can dramatically change the mean momentum balance, resulting in Langmuir circulations, or the turbulence balance as shown by Cheung & Street (1988) and can have very strong consequences. Since, vorticity is very sensitive to the gradient of velocity, it is very sensible to describe the high Reynolds number flow in terms of vorticity. Moreover, the action of the viscous force can be observed in terms of higher vorticity and shear stress. Hence the question arises whether there is any presence of vorticity and shear stress in the progressive water waves without wind, i.e. progressive water waves with air following the water waves. If so, what is the maximum value of the vorticity and shear stress in the water waves? Are they symmetrical under the crest and trough? How does the structure and the behaviour of vorticity and shear stress change with varying water depth and how does it affect our understanding of wave dynamics? Current work is an attempt to address these questions related to the structure and the behaviour of vorticity and

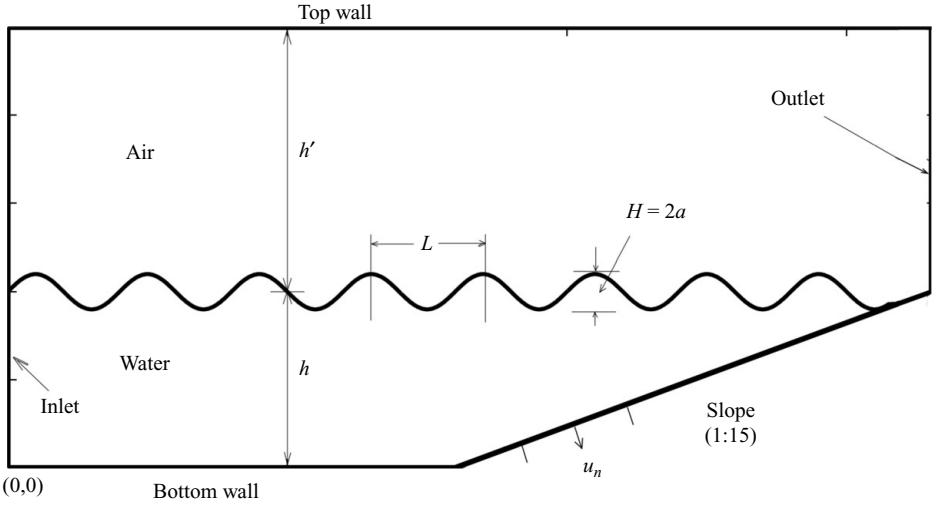

FIGURE 1. Sketch of the domain used in the simulation.

shear stress in non-breaking, nonlinear, transient and viscous water waves. Numerical simulation is essential to answer such questions since there is very little experimental measurement due to the complex nature of the water waves.

Section 2 details on the problem formulation and the governing equations. Section 3 describes the numerical method and the simulation parameters used in the calculation. Section 4 discusses numerical results. Section 5 summarizes the paper and draws conclusions from the numerical simulation results and their implications.

2. Problem formulation

The water wave under investigation is modelled as a two-dimensional viscous, transient and progressive water wave as outlined in figure 1. The frame of reference for our computations and analysis is a fixed cartesian coordinate system and is aligned to the bottom of the solution domain near the inlet specified as $(x, y) = (0, 0)$ as shown in figure 1. The water waves are continuously generated at the inlet on the left end of the domain and allowed to travel along the positive x direction and dissipate on a beach at the far right end of the domain. The air present above is 'moving' and follows the motion of water and the average wind velocity is set to be zero. The wavelength in the problem is given by L, periodic time is T, wave amplitude is a, wavenumber is $k = 2\pi/L$, angular frequency is $\sigma = 2\pi/T$, wave phase speed is $c = L/T = \sigma/k$, wave steepness $= 2a/L$, depth of water is h and depth of air is h'. According to Zwart *et al.* (2007) the free surface flow can be considered as a special case of two-phase flow where water and air can be described as phase 1 and phase 2 respectively. Hence, the governing equations can be described in the form similar to two-phase flow as described in Kleinstreuer (2003, pp. 198–201), Drew & Passman (1999, pp. 68–83). In the two-dimensional unsteady flow, the full Navier–Stokes equations are given by the continuity equation for water:

$$\frac{\partial}{\partial t}(\rho_w f_w) + \frac{\partial}{\partial x}(\rho_w f_w u) + \frac{\partial}{\partial y}(\rho_w f_w v) = 0, \tag{2.1}$$

the continuity equation for air:

$$\frac{\partial}{\partial t}(\rho_a f_a) + \frac{\partial}{\partial x}(\rho_a f_a u) + \frac{\partial}{\partial y}(\rho_a f_a v) = 0, \tag{2.2}$$

the momentum equation in the x direction:

$$\frac{\partial}{\partial t}(\rho_m u) + \frac{\partial}{\partial x}(\rho_m uu) + \frac{\partial}{\partial y}(\rho_m vu) = -\frac{\partial p}{\partial x} + \frac{\partial}{\partial x}\left(\mu_m \frac{\partial u}{\partial x}\right) + \frac{\partial}{\partial y}\left(\mu_m \frac{\partial u}{\partial y}\right) \tag{2.3}$$

and in the y direction:

$$\frac{\partial}{\partial t}(\rho_m v) + \frac{\partial}{\partial x}(\rho_m uv) + \frac{\partial}{\partial y}(\rho_m vv) = -\frac{\partial p}{\partial y} + \frac{\partial}{\partial x}\left(\mu_m \frac{\partial v}{\partial x}\right) + \frac{\partial}{\partial y}\left(\mu_m \frac{\partial v}{\partial y}\right) - \rho_m g, \tag{2.4}$$

where the velocity components are given by u and v at each point in space, pressure is p and g is acceleration due to gravity. f_w, ρ_w and μ_w represent the volume fraction, density and viscosity of water, respectively, and f_a, ρ_a and μ_a represent the volume fraction, density and viscosity of the air, respectively. Therefore, in air $f_a = 1$, $f_w = 0$, in water $f_a = 0$, $f_w = 1$ and in the cell which contains free surface $0 < f_a < 1, 0 < f_w < 1$.

Mixture density ρ_m and mixture viscosity μ_m are calculated by

$$\rho_m = \rho_w f_w + \rho_a f_a, \tag{2.5}$$

$$\mu_m = \mu_w f_w + \mu_a f_a. \tag{2.6}$$

The volume continuity constraint requires that the volume fractions of air and water must sum to unity, hence

$$f_w + f_a = 1. \tag{2.7}$$

2.1. *Initial and Boundary conditions*

For the domain shown in the figure 1, when there is no current in water and air, the solution of the potential flow in the solution domain is given in Milne-Thomson (1994). The surface elevation η of the wave travelling in the x direction is

$$\eta = a \ \sin k(x - ct). \tag{2.8}$$

The velocity components, pressure and volume of fractions in the water and air are calculated using complex potential and in the water they are given by

$$u = a\,k\,(c)\,\frac{\sin k(x - ct)\,\cosh ky}{\sinh kh}, \tag{2.9a}$$

$$v = a\,k\,(-c)\,\frac{\cos k(x - ct)\,\sinh ky}{\sinh kh}, \tag{2.9b}$$

$$p = \rho_w \left[a\,k\,c^2 \frac{\sin k(x - ct)\,\cosh ky}{\sinh kh}\right] - \rho_w(u^2 + v^2) - \rho_w g(y - h), \tag{2.10}$$

$$f_w = 1, \qquad f_a = 0 \tag{2.11}$$

and in the air are given by

$$u = ak(-c)\frac{\sin k(x - ct)\cosh k(y - h' - h)}{\sinh kh'}, \tag{2.12a}$$

$$v = ak(c)\frac{\cos k(x - ct)\sinh k(y - h' - h)}{\sinh kh'}, \tag{2.12b}$$

$$p = \rho_a \left[-a\,k\,c^2 \frac{\sin k(x - ct)\,\cosh k(y - h' - h)}{\sinh kh} \right] - \rho_a(u^2 + v^2) - \rho_a g y, \tag{2.13}$$

$$f_w = 0, \quad f_a = 1. \tag{2.14}$$

2.1.1. *Initial conditions*

The initial conditions for the air and water are calculated using the equations for pressure and velocity in the air and water of the potential flow. Hence, we substitute $t = 0$ into (2.8)–(2.14) to get the initial distributions in the domain. The use of the analytical solution as the initial conditions can substantially reduce the computational effort.

2.1.2. *Boundary conditions*

At the inlet the boundary conditions for water and air are calculated by substituting $x = 0$ into (2.8), (2.9) and (2.12). On the top, bottom and slope a no-slip wall boundary is applied in agreement with experimental set-up of Mitsuyasu & Honda (1982). At the outlet an opening boundary condition is applied. Due to the asymmetry of velocity resulting in more fluid moving in the wave direction under the wave crest than moving out under the trough region, there is a mean transport of water from the inlet and it is calculated by

$$Q = \frac{1}{T} \int_t^{t+T} \int_0^{h+\eta} u \,\mathrm{d}y \,\mathrm{d}t = \frac{ac}{T \sinh(kh)} \int_t^{t+T} \sinh[kh + ak \sin(-\sigma t)] \sin(-\sigma t) \,\mathrm{d}t, \tag{2.15}$$

and it is taken out by setting an outflow u_n boundary condition on the slope, as seen in figure 1.

3. Numerical model and simulation parameters

3.1. *Numerical model*

3.1.1. *Domain discretization*

The conservation equations described earlier are discretized using an element-based finite volume method developed by Schneider & Raw (1987). A control volume is constructed around each mesh vertex as seen in figure 2. The subface between two control volumes within a particular element is called an *integration point* (ip) where the fluxes are discretized. Pressure and velocity gradients are obtained from vertex values using finite element shape functions.

3.1.2. *Equation discretization and solution strategy*

Conservation equations (2.1)–(2.4) are discretized at each control volume. The conservation equations are integrated over each control volume, the volume integrals are converted to surface integrals using Gauss' divergence theorem. When the implicit second-order backward Euler scheme is used for the time derivative, the discrete representations of (2.1) and (2.2) in the water and air are

$$\frac{V}{\delta t} \left(\frac{3}{2}(\rho_w f_w)^{n+1} - 2(\rho_w f_w)^n + \frac{1}{2}(\rho_w f_w)^{n-1} \right) + \sum_{ip} (\rho_w u^j A^j)_{ip}^{n+1} (f_{w,ip})^{n+1} = 0, \tag{3.1a}$$

$$\frac{V}{\delta t} \left(\frac{3}{2}(\rho_a f_a)^{n+1} - 2(\rho_a f_a)^n + \frac{1}{2}(\rho_a f_a)^{n-1} \right) + \sum_{ip} (\rho_a u^j A^j)_{ip}^{n+1} (f_{a,ip})^{n+1} = 0. \tag{3.1b}$$

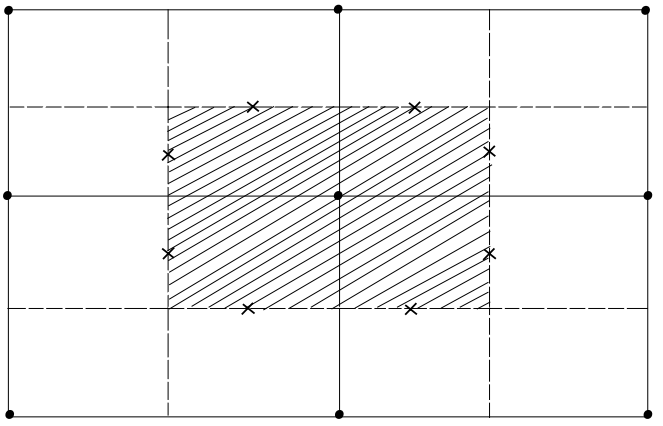

FIGURE 2. Element based finite volume discretization. Solid lines are element boundaries and dashed lines divide the elements into parts. Black dots (•) represent solution unknowns at the vertices and cross (×) represents integration points where surface fluxes are evaluated. Shaded region is control volume around each vertex.

The discrete representations of (2.3) (2.4) are given by

$$\frac{\rho_m V}{\delta t}\left(\frac{3}{2}u_{ip}^{n+1}-2u_{ip}^{n}+\frac{1}{2}u_{ip}^{n-1}\right)+\sum_{ip}(\rho_m u_{ip}^{j}A^{j})^{n+1}u_{ip}^{n+1} = -\sum_{ip}\left(p_{ip}^{n+1}A^{1}\right)_{ip}+\sum_{ip}\left(\left(\tau_m^{ji}\right)^{n+1}A^{j}\right)_{ip}, \quad (3.2a)$$

$$\frac{\rho_m V}{\delta t}\left(\frac{3}{2}v_{ip}^{n+1}-2v_{ip}^{n}+\frac{1}{2}v_{ip}^{n-1}\right)+\sum_{ip}\left(\rho_m u_{ip}^{j}A^{j}\right)^{n+1}v_{ip}^{n+1} = -\sum_{ip}\left(p_{ip}^{n+1}A^{2}\right)_{ip}-\rho_m^{n+1}g^{i}V+\sum_{ip}\left(\left(\tau_m^{ji}\right)^{n+1}A^{j}\right)_{ip}, \quad (3.2b)$$

where, $j=1,\ 2$ gives $u_{ip}^{1}=u_{ip}$ and $u_{ip}^{2}=v_{ip}$, V represents the volume of a control volume, A_{ip}^{j} the area vector of a subface corresponding to an integration point, δt the time step and the superscripts $n+1$, n and $n-1$ means that the quantity is evaluated at the new and earlier time steps. The advection scheme used to evaluate $f_{w,ip},\ f_{a,ip},\ u_{ip}$ and v_{ip} in term of neighbouring vertex values is written in the form

$$\phi_{ip}=\phi_{up}+\beta\nabla\phi\cdot\boldsymbol{R}, \quad (3.3)$$

where ϕ_{up} is the upwind vertex value and $\boldsymbol{R}$ is the vector from the upwind vertex to the integration point, $\nabla\phi$ is calculated by the nodal gradient of the upwind node. For the momentum equations (3.2a) and (3.2b) the second-order upwind biased scheme is used by setting $\beta=1$. For the continuity equations (3.1a) and (3.1b), a high resolution scheme is used by setting β and ϕ_{ip} is bounded by the maximum and minimum values of ϕ among the vertex's neighbours. This scheme is developed by Barth & Jesperson (1989) and is compared with other high resolution schemes by Darwish & Moukalled (2003). The mass flow flux is calculated using pressure smoothing technique for flux through the face of control volume developed by Rhie & Chow (1983). The

discretization technique has been used in the past by Zwart (2005), Zwart, Scheuerer & Bogner (2003) and Corte & Grilli (2006).

The set of equations (2.7), (3.1) and (3.2) represents equations for volume fraction, velocity and pressure fields along with two phases forming a coupled system of equations at each control volume. Assembled into the global system, these coupled system of equations are solved simultaneously by using an algebraic multigrid method developed by Hutchinson & Raithy (1986) and Raw (1996).

3.2. *Simulation parameters*

The domain in the numerical simulations is similar to the one used in experimental study by Mitsuyasu & Honda (1982). The size of the domain is 11 m long and 0.8 m high, the depth of the water is $h = 0.335$ m and the depth of the air is $h' = 0.465$ m, a further increase of the length of domain increases the computational work but has little effect on the solutions in the region $x = 3$–6 m. The slope of the beach is $1/15$ which has been used in the experimental investigation in the past by Peirson, Garcia & Pells (2003) to minimize the reflection from the right end of the domain. A structured mesh is used for grid generation and near the free surface 16 grid points are distributed in vertical direction in the wave height. In the air and under the water a non-uniform mesh is used. One hundred grid points are uniformly distributed in the x direction per wavelength which produces mesh independent results. The wavelength for the water wave is calculated using a dispersion relation given by $\sigma^2 = gk \tanh(kh)$.

We consider six cases some of which are described in the work of Mitsuyasu & Honda (1982) for the purpose of comparison, three cases for deep water waves and three cases for intermediate depth water waves of varying steepnesses. These six different cases will help validate the numerical results across a broad spectrum of wave steepness and water depth which are of interest to oceanographers and hydrodynamicists. Case 1 (C1) is the intermediate depth water wave in which the wave steepness is $2a/L = 0.04$, $h/L = 0.2$ and $T = 0.7592$ s. Case 2 (C2) is the deep water wave in which the wave steepness is 0.04, $h/L = 0.6$ and $T = 0.6$ s. Case 3 (C3) is intermediate depth water wave with a wave steepness of 0.06, $h/L = 0.2$ and $T = 0.7592$ s. Case 4 (C4) is a deep water wave with a wave steepness of 0.06, $h/L = 0.6$ and $T = 0.6$ s. Case 5 (C5) is an intermediate depth water wave case with wave steepness of 0.08, $h/L = 0.2$ and $T = 0.7592$ s and Case 6 (C6) is an deep water wave with wave steepness of 0.08, $h/L = 0.6$ and $T = 0.6$ s. In order to compare with the experiment an additional case for intermediate depth water waves (C_{ex}) is also included for discussion of energy density variation along the domain. The wave steepness in this case is $2a/L = 0.06$, $h/L = 0.44$ and $T = 0.7$ s. The maximum wave steepness is set at 0.08, the waves are about to break when the wave steepness increases further. All calculations are performed under zero average wind speed and little velocity fluctuation has been found in the water, therefore the analysis focus on laminar flow.

4. Numerical results and discussion

4.1. *Energy density*

In order to investigate the effect of viscosity on the decay rate of water wave and validate the numerical calculations we compare the numerically calculated decay rate of water wave with the experimental measurement. A potential energy density factor

α_{PE} is defined by

$$\alpha_{PE} = \frac{\overline{PE}}{E_0}, \tag{4.1}$$

where potential energy density for a progressive wave is given by

$$\overline{PE} = \frac{1}{L}\int_x^{x+L} \frac{\rho_w g \eta^2}{2}\,\mathrm{d}x, \tag{4.2}$$

where E_0 is the total energy at the inlet and is given by

$$E_0 = \frac{1}{2}\,\rho_w g a^2. \tag{4.3}$$

The kinetic energy density factor in the water waves is

$$\alpha_{KE} = \frac{\overline{KE}}{E_0}, \tag{4.4}$$

where kinetic energy density is given by

$$\overline{KE} = \frac{1}{L}\int_x^{x+L}\int_0^{h+\eta} \rho_w \left(\frac{u^2+v^2}{2}\right)\mathrm{d}x\,\mathrm{d}y. \tag{4.5}$$

The total energy density factor is the sum of the potential energy density factor and the kinetic energy density factor and is given by

$$\alpha_T = \alpha_{PE} + \alpha_{KE}. \tag{4.6}$$

The time averaged results for the total, potential and kinetic energy density factors are calculated by

$$\overline{\alpha}_T = \frac{1}{T}\int_0^T \alpha_T\,\mathrm{d}t, \tag{4.7}$$

$$\overline{\alpha}_{PE} = \frac{1}{T}\int_0^T \alpha_{PE}\,\mathrm{d}t, \tag{4.8}$$

$$\overline{\alpha}_{KE} = \frac{1}{T}\int_0^T \alpha_{KE}\,\mathrm{d}t. \tag{4.9}$$

On comparing the time averaged numerical results for the total, potential and kinetic energy density factors in the intermediate depth water waves (case C_{ex}, figure 3) and deep water waves (case C4, figure 4), we found that the numerical results are in good agreement with theoretical and experimental results described in Mitsuyasu & Honda (1982). The most noticeable difference observed is the wave energy density decay rate in both cases for the same water depth. The deep water wave shows higher decay rate than the intermediate depth water wave over the same distance travelled since the deep water has more waves than the intermediate depth water over the same length of the solution domain. This can be seen in table 1 which shows the decay rate Δ calculated from the time averaged total energy density factor, by fitting the relationship

$$\frac{\overline{E}}{\overline{E}_0} = \overline{\alpha}_T = \exp(-\Delta x). \tag{4.10}$$

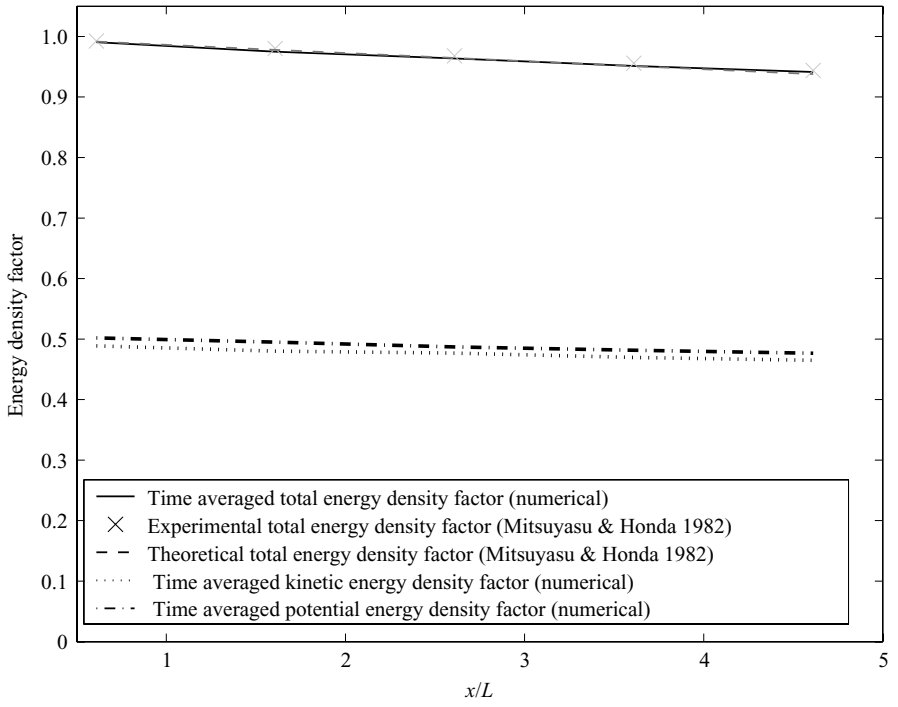

FIGURE 3. Time averaged energy density factor versus x; case C_{ex}, $2a/L = 0.06$, $h/L = 0.4$.

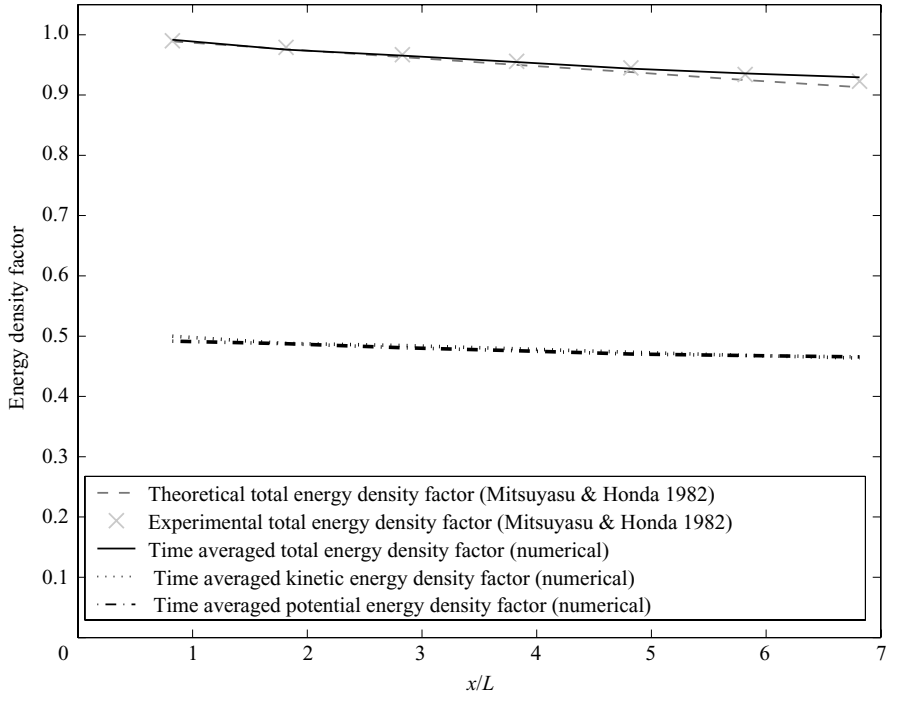

FIGURE 4. Time averaged energy density factor versus x; case C4, $2a/L = 0.06$, $h/L = 0.6$.

H/L	T (s)	Δ_{theory}	Δ_{exp}	Δ_{num}
0.06	0.7	1.83×10^{-4}	1.65×10^{-4}	1.727×10^{-4}
0.06	0.6	2.38×10^{-4}	2.10×10^{-4}	1.914×10^{-4}

TABLE 1. Exponential decay rate Δ; $E = E_0 \exp(-\Delta x)$.

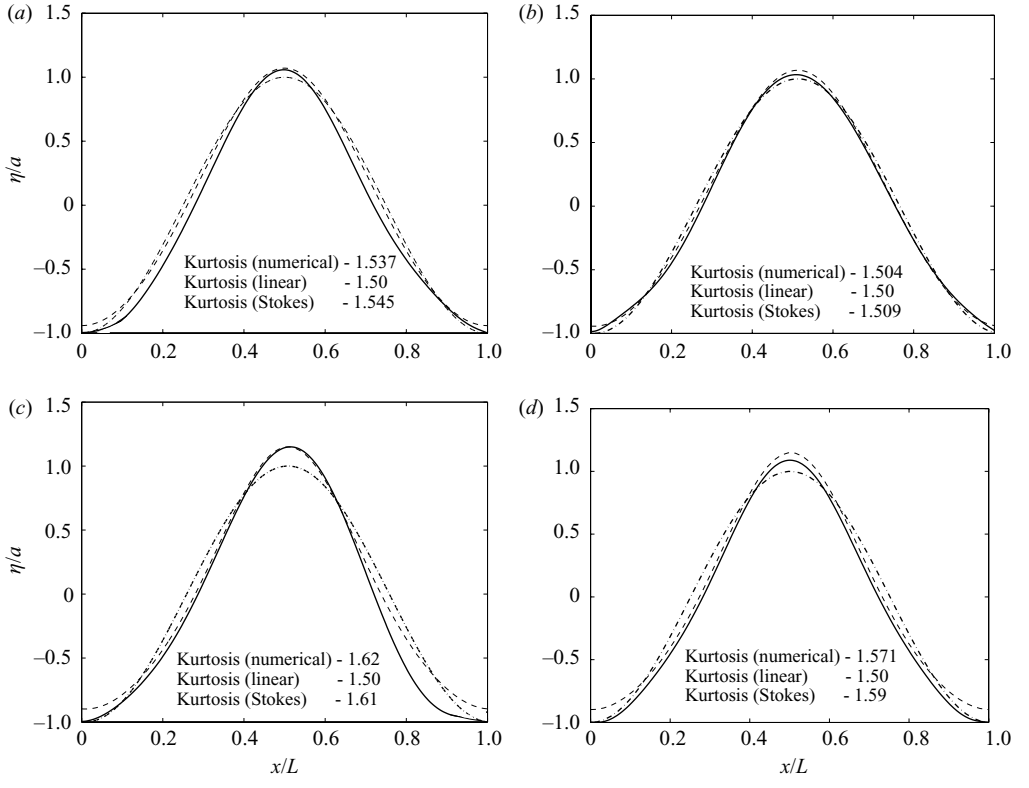

FIGURE 5. Free surface in the potential flow versus viscous flow for cases (*a*) C1: $2a/L = 0.04$, $h/L = 0.2$; (*b*) C2: $2a/L = 0.04$, $h/L = 0.6$ (*c*) C5: $2a/L = 0.08$, $h/L = 0.2$ and (*d*) C6: $2a/L = 0.08$, $h/L = 0.6$; —, the numerical result; $- \cdot -$, the potential flow; $- - -$, the Stokes wave.

Theoretical and experimental values of Δ (Δ_{theory} and Δ_{exp}) are from Mitsuyasu & Honda (1982). The decay rate calculated from numerical results (Δ_{num}) show very good agreement with the theoretical and experimental values.

To better understand the physics leading to the difference in decay rate, we analyse various aspects of viscous, nonlinear, rotational and transient water waves in the following sections.

4.2. *Free surface comparison*

The comparison of the profiles of the free surfaces produced by the potential flow, the Stokes wave and the numerical calculations for the intermediate depth water waves cases C1 and C5 and deep water waves cases C2 and C6 is made in figure 5. The

kurtosis of these wave profiles is quantified by following formula:

$$k = \frac{\Sigma_{i=1}^{N}(\eta - \bar{\eta})^4}{(N-1)s^4}, \tag{4.11}$$

where $\bar{\eta}$ is the mean of η, s is the standard deviation of η and N represents the number of data points. In the cases of small wave steepness cases C1 and C2 ($2a/L = 0.04$), the Stokes flow and numerical solutions have a flatter surface in the trough and a sharper crest near the peak of the wave as compared to potential flow, consequently they have larger kurtosis than the potential flow. It is an expected behaviour due to nonlinearity of water wave, which causes the wave to loose the sinusoidal shape leading to sharper crest and flatter trough. The Stokes wave and numerical results also produce an increase in the free surface location near the peak because when the trough becomes flatter the water mass is moved to crest in order to maintain the mass conservation, which leads to a higher crest. In the cases of large wave steepness C5 and C6 ($2a/L = 0.08$), the kurtosis of the Stokes wave and numerical solution increases further, therefore, the flat surface near the trough extends further horizontally and the crest becomes even sharper and hence the effect of nonlinearity has become much significant. The intermediate depth water waves in cases C1 and C5 have more steeper surface at the crest than deep water wave mainly due to displacement from the bottom boundary forcing the water to move towards the crest region. We also observe from figure 5(c) that the intermediate depth water wave starts loosing its symmetry with the increase in the wave steepness, and a small forward bending of the wave is seen due to the effect of bottom whereas the deep water waves in figure 5(d), on the other hand, tend to be symmetrical and have the wave profile similar to linear potential flow and nonlinear Stokes wave.

4.3. *Velocity vectors and streamlines in the water waves*

4.3.1. *Velocity vectors*

The velocity is non-dimensionalized is calculated as

$$\overline{u} = \frac{u}{akc}, \tag{4.12}$$

$$\overline{v} = \frac{v}{akc}. \tag{4.13}$$

In figure 6, a typical velocity vector distributions in the water show the periodic feature of the waves. To investigate further, velocity distributions in cases C3 and C4 are plotted in figures 8 and 10 and compared with the analytical solutions of the corresponding potential flows in figures 7 and 9. The contours of velocity magnitude for cases C3 and C4 as per the analytical solutions of the potential flow and the numerical results for the viscous flow are also shown in figures 7–10, respectively. On comparing these results, we observe that for the viscous flow in figures 8 and 10 the velocity contours with the values which are lower than 0.8 move to higher locations; this indicates that in most lower parts of the water wave, the velocity of the viscous flow is lower than the potential flow because of the resistance from the viscosity. We also observe that in the cases of the viscous flows the velocity becomes higher in the crest than the potential flow because the resistance from the friction in the water decreases from the water into the air and this allows a higher velocity in the crest. In the case of intermediate depth water wave as seen in figure 8, an increase in the

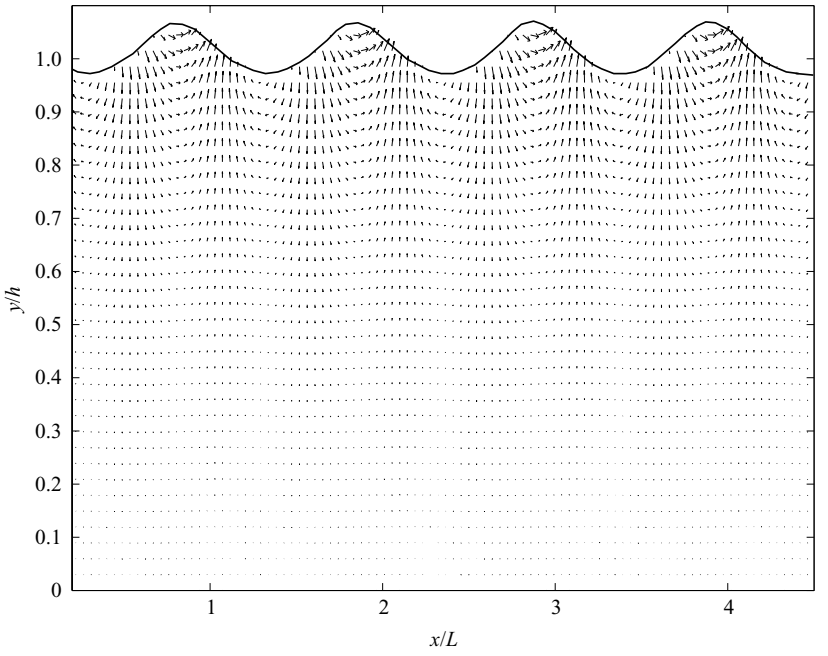

FIGURE 6. Non-dimensional velocity vectors in the domain of viscous flow.

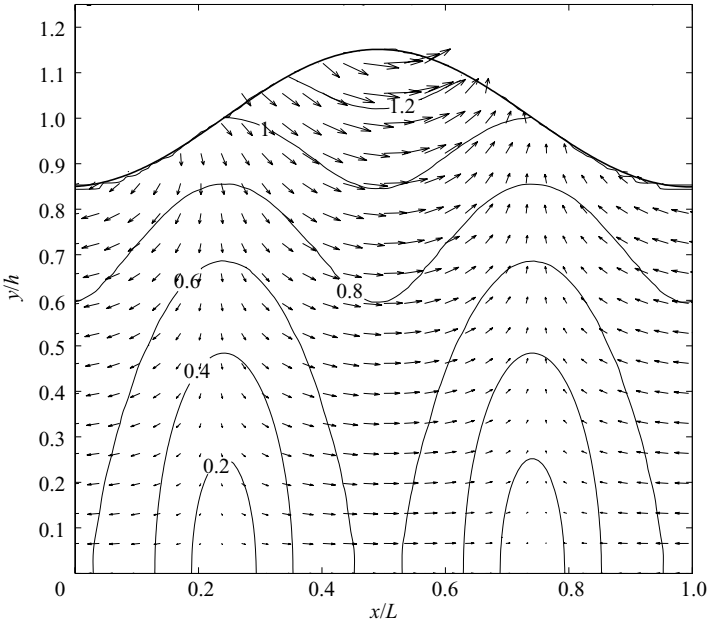

FIGURE 7. Non-dimensional velocity vectors with velocity contours in a typical wave of potential flow; case C3: $2a/L = 0.06$, $h/L = 0.2$.

maximum velocity near the crest of the viscous flow is about 66 %, which is double compared with an increase in figure 10 in deep water wave of 33 %, indicating that bottom boundary can increase velocity near the crest substantially.

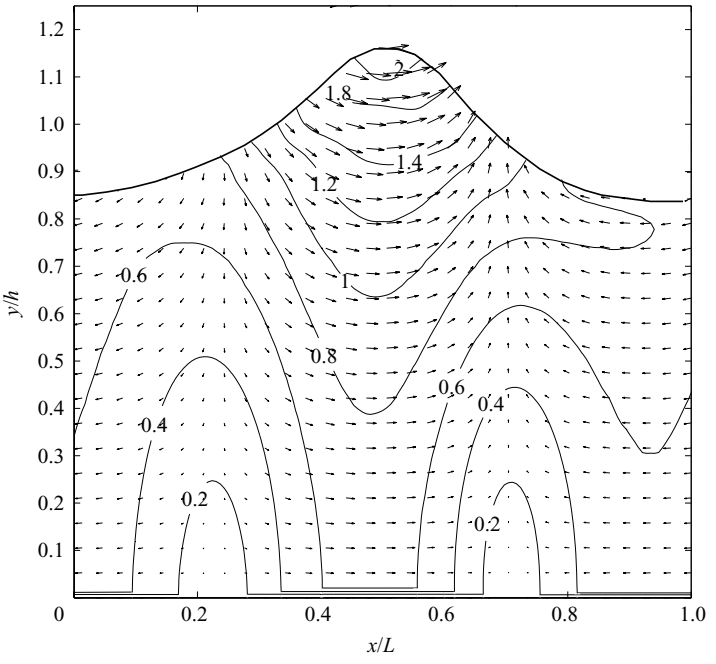

FIGURE 8. Non-dimensional velocity vectors with velocity contours in a typical wave of viscous flow; case C3: $2a/L = 0.06$, $h/L = 0.2$.

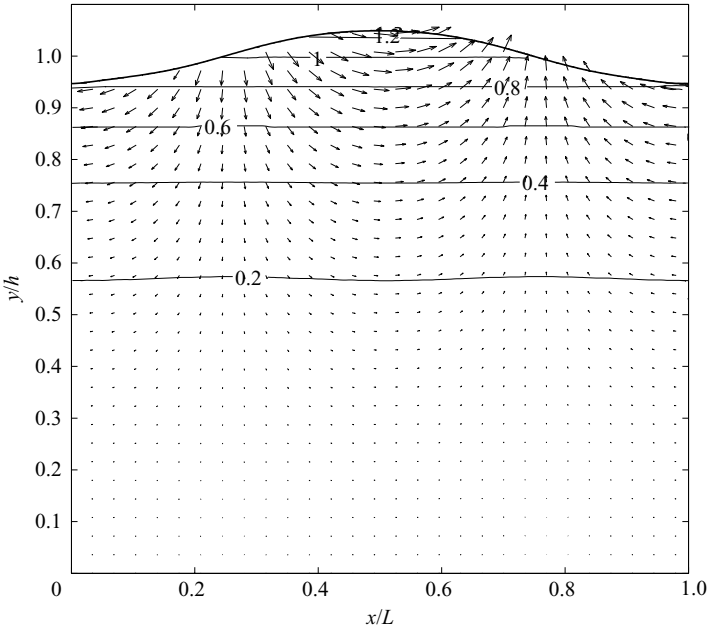

FIGURE 9. Non-dimensional velocity vectors with velocity contours in a typical wave of potential flow; case C4: $2a/L = 0.06$, $h/L = 0.6$.

4.3.2. *Streamlines*

To investigate further we plot streamlines in the water waves. The stream function ψ is non-dimensionalized by wave amplitude a and wave speed c:

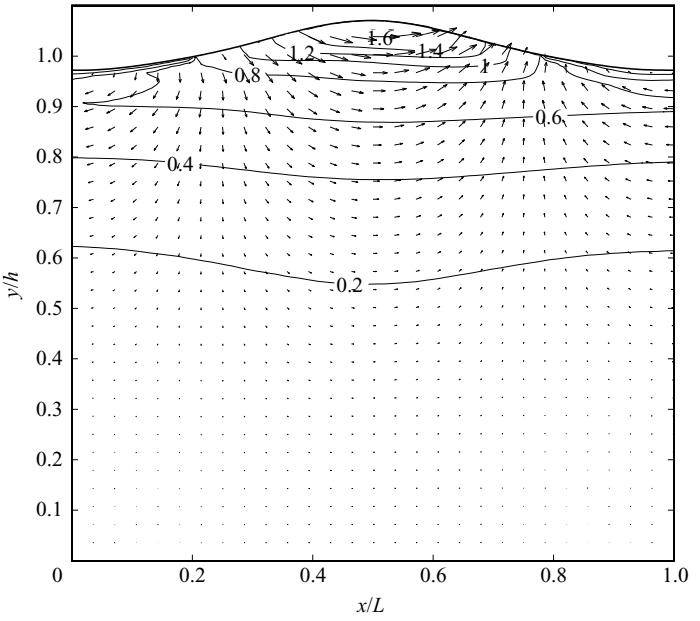

FIGURE 10. Non-dimensional velocity vectors with velocity contours in a typical wave of viscous flow; case C4: $2a/L = 0.06$, $h/L = 0.6$.

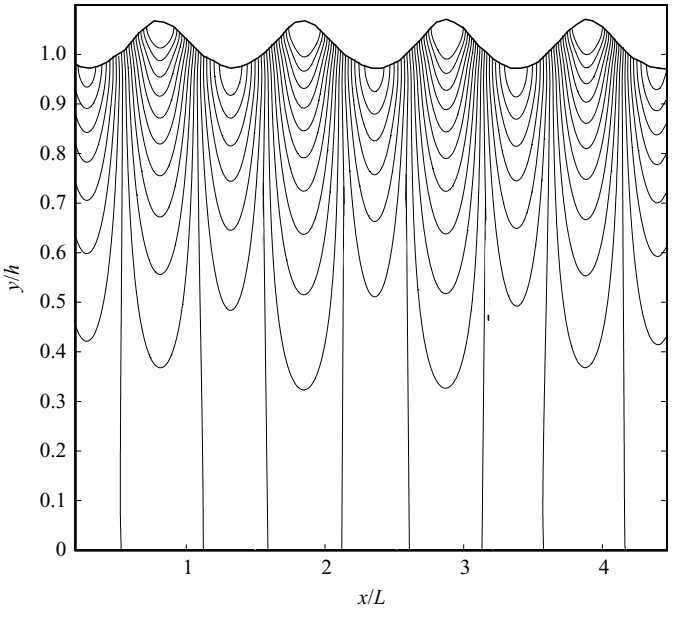

FIGURE 11. Streamlines in the domain of viscous flow.

$$\overline{\psi} = \frac{\psi}{ac}. \tag{4.14}$$

Figure 11 shows instantaneous streamlines in the domain of case C4. It mostly shows periodic and symmetric distribution of streamlines in the domain. For further analysis, figures 12 and 14 show the streamlines in cases C3 and C4 produced by

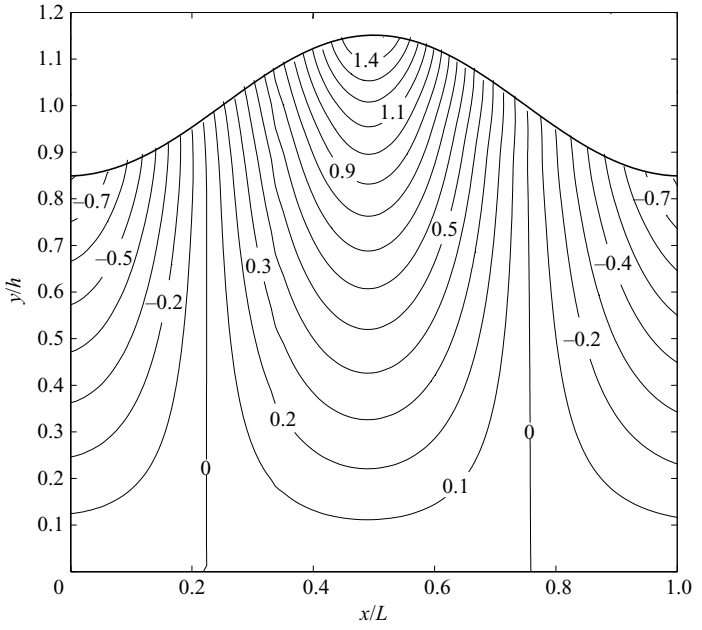

FIGURE 12. Streamlines in a typical wave of potential flow; case C3: $2a/L = 0.06$, $h/L = 0.2$.

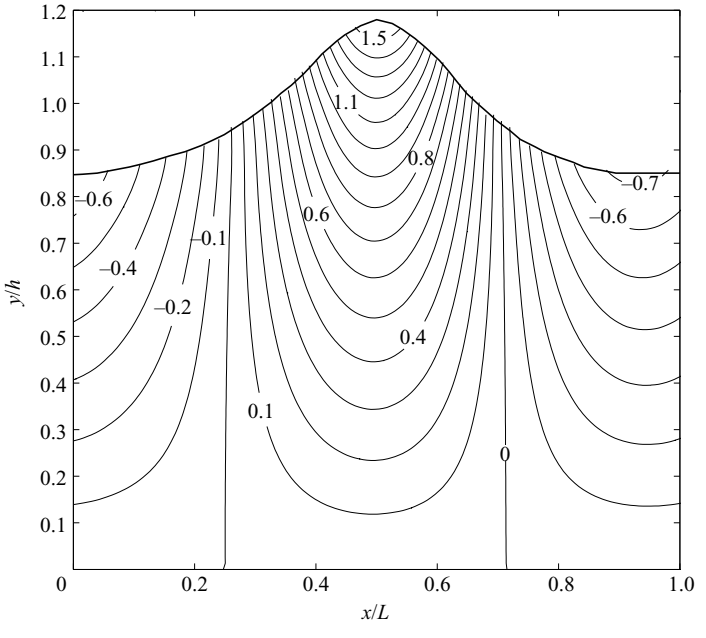

FIGURE 13. Streamlines in a typical wave of viscous flow; case C3: $2a/L = 0.06$, $h/L = 0.2$.

the analytical solution of the potential flow. Figures 13 and 15 show the streamlines produced by the numerical simulations of the nonlinear viscous flow. Similar to the velocity contours, the streamlines of the viscous flow in most parts of the domain are located at higher places than those of the potential flow. Under the trough, the

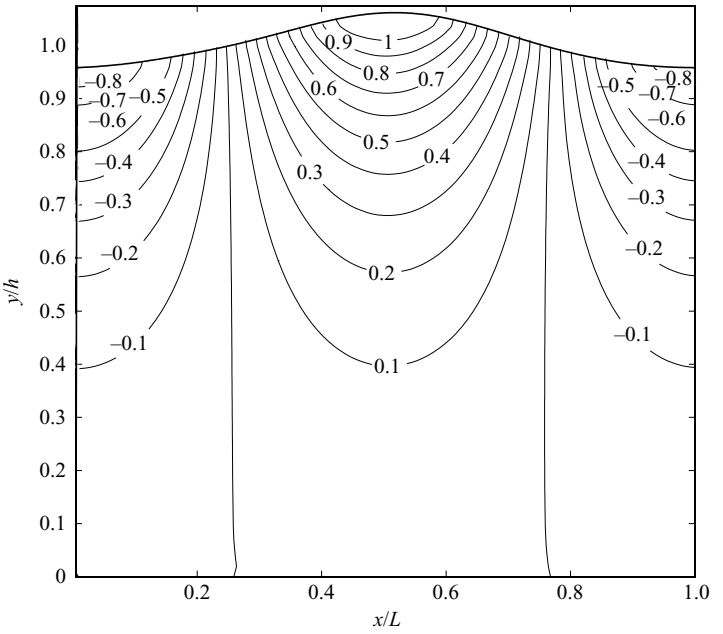

FIGURE 14. Streamlines in a typical wave of potential flow; case C4: $2a/L = 0.06$, $h/L = 0.6$.

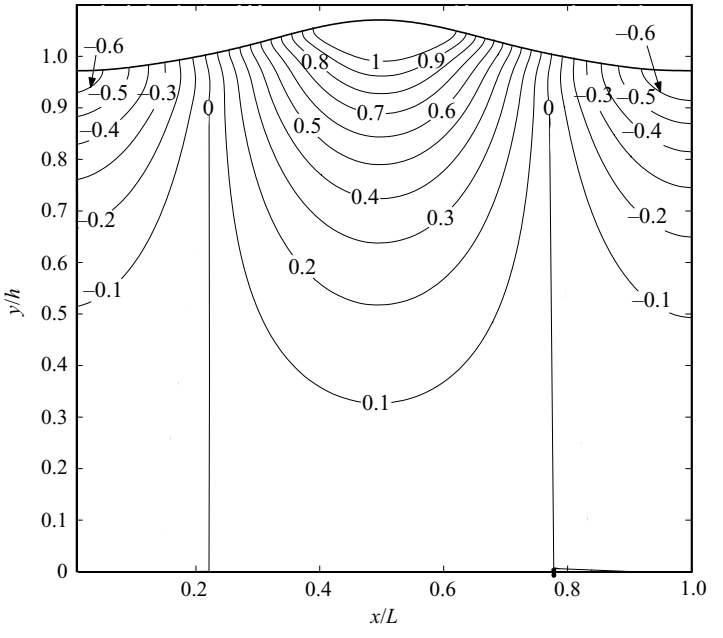

FIGURE 15. Streamlines in a typical wave of viscous flow; case C4: $2a/L = 0.06$, $h/L = 0.6$.

viscous flow has smaller negative maximum values for the stream function and under the crest it has higher positive maximum values. This indicates that the fluid tries to move towards the crest where it encounters less resistance. All the numerically produced instantaneous streamlines in figures 13 and 15 and all other cases are very

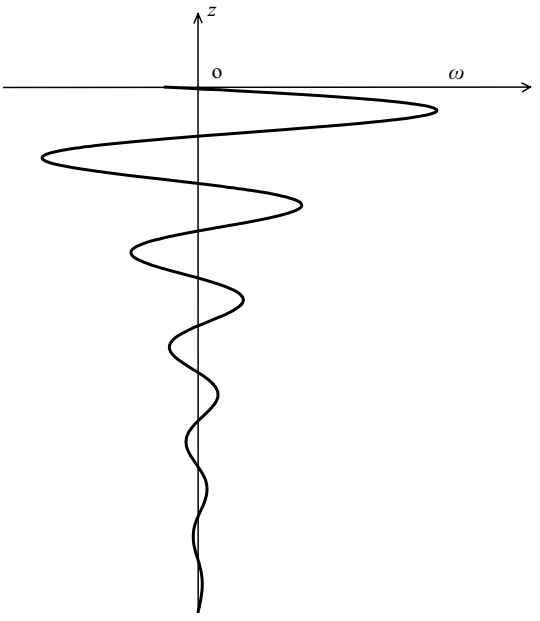

FIGURE 16. A representation of the behaviour of the vorticity field with depth given by (4.17).

smooth and regularly distributed, these are the evidences of laminar flows in the water presented in this paper.

4.4. *Vorticity field*

We now investigate the vorticity in the domain. Numerical results of the vorticity are obtained after solving the full Navier–Stokes equations for the unsteady, nonlinear and viscous water waves. In order to reveal the characteristics of the viscous flow, it is desirable to calculate the vorticity at every point under the wave and this is given by

$$\omega = \frac{\partial v}{\partial x} - \frac{\partial u}{\partial z}, \tag{4.15}$$

where $z = y - h$, while the non-dimensional vorticity is defined as

$$\overline{\omega} = \omega/(2ak\sigma). \tag{4.16}$$

According to Kinsman (1965) and Lamb (1932), for a low-Reynolds-number flow, the analytical solution for the vorticity in water wave with small amplitude is given by

$$\omega = -2ak\sigma \mathrm{e}^{\left\{\left(\frac{\sigma}{2\nu}\right)^{\frac{1}{2}} z - \frac{2\sigma}{R_w} t\right\}} \cos\left[kx + \left(\frac{\sigma}{2\nu}\right)^{\frac{1}{2}} z + \sigma t\right], \tag{4.17}$$

where ν is the kinematic viscosity of the fluid and R_w is the wave Reynolds number, which is defined as

$$R_w = \frac{\sigma}{\nu k^2}. \tag{4.18}$$

The behaviour of the vorticity field given by (4.17) is sketchily shown in figure 16. We can see that the vorticity is damped to zero exponentially in an oscillatory manner with increase in the water depth and this analytical solution has revealed an important fact that the oscillation of vorticity is caused by the viscosity.

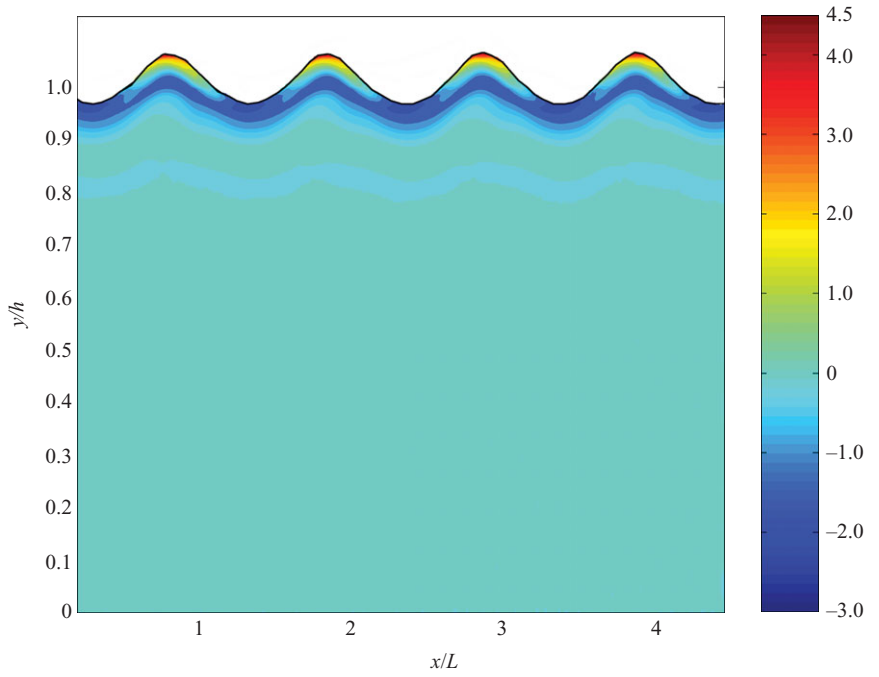

FIGURE 17. Non-dimensional vorticity ($\overline{\omega}$) of case C4: $2a/L = 0.06$, $h/L = 0.6$.

The vorticity profile produced by the inviscid rotational Gerstner wave (Gerstner 1802) can be found from Lamb (1932):

$$\omega = -\frac{2a^2k^2\sigma e^{2kz_0}}{1 - a^2k^2e^{2kz_0}}, \tag{4.19}$$

where z_0 is a parameter given by

$$x = \frac{\theta}{k} + ae^{kz_0}\sin\theta, \tag{4.20}$$

$$z = z_0 - ae^{kz_0}\cos\theta. \tag{4.21}$$

The vorticity is damped in the Gerstner's wave (Gerstner 1802) but does not produce oscillations, which indicates that water rotates in the same direction in the whole domain.

A typical numerical result for the vorticity field under the water waves for case C4 is shown in figure 17. It reveals the oscillatory distribution of the vorticity, which indicates that water rotates in different directions in different parts of the domain. In this figure we observe a periodic thick layer of active vorticity near the water surface. The magnitude of the vorticity becomes smaller and reduces to zero with the increase in depth. In the all six cases the global distributions of vorticity are similar to figure 17.

We now reveal the details of vorticity for the deep water waves (cases C2 and C6) and intermediate depth water waves (cases C1 and C5) with varying steepness. In figures 18–21 we see a similar vorticity distributions in all cases. Along the water surface, the vorticity changes from negative maximum at the trough to positive maximum at the crest. The vorticity in the crest and trough is different in direction signifying the 'anticlockwise' and 'clockwise' rotation of the fluid respectively. This

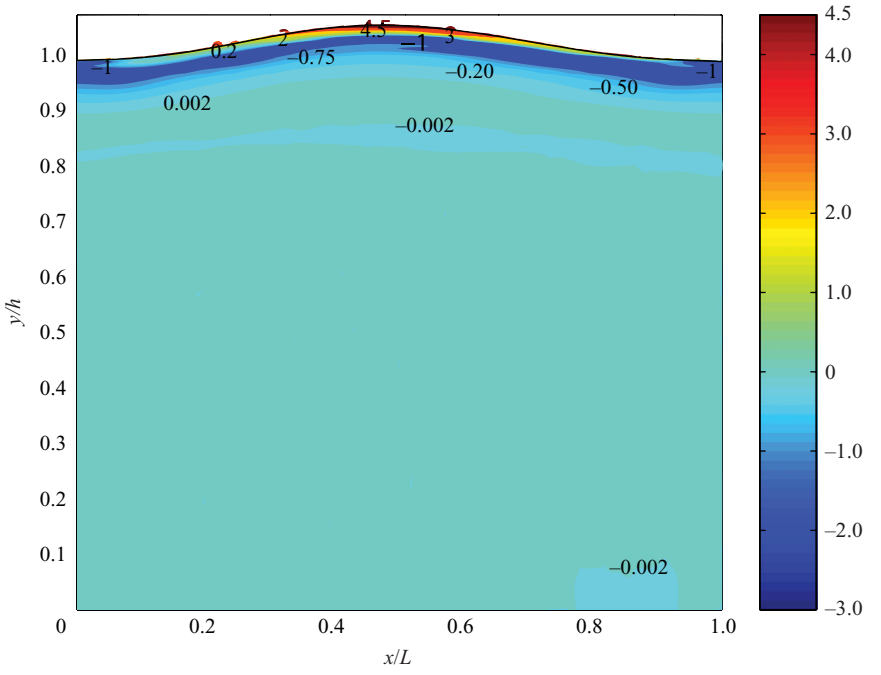

FIGURE 18. Non-dimensional vorticity ($\overline{\omega}$) in a typical wave of case C2: $2a/L = 0.04$, $h/L = 0.6$.

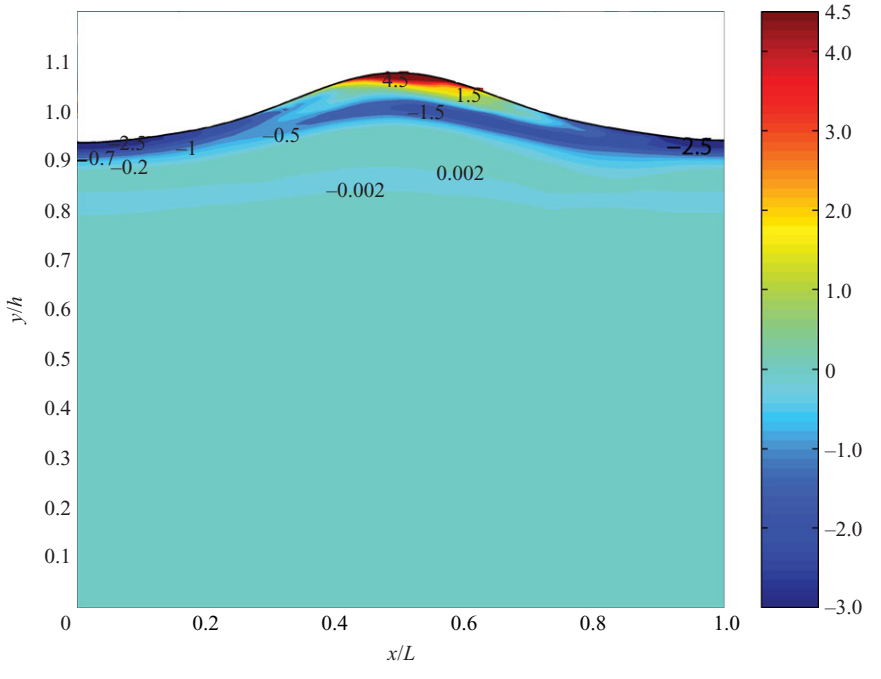

FIGURE 19. Non-dimensional vorticity ($\overline{\omega}$) in a typical wave of case C6: $2a/L = 0.08$, $h/L = 0.6$.

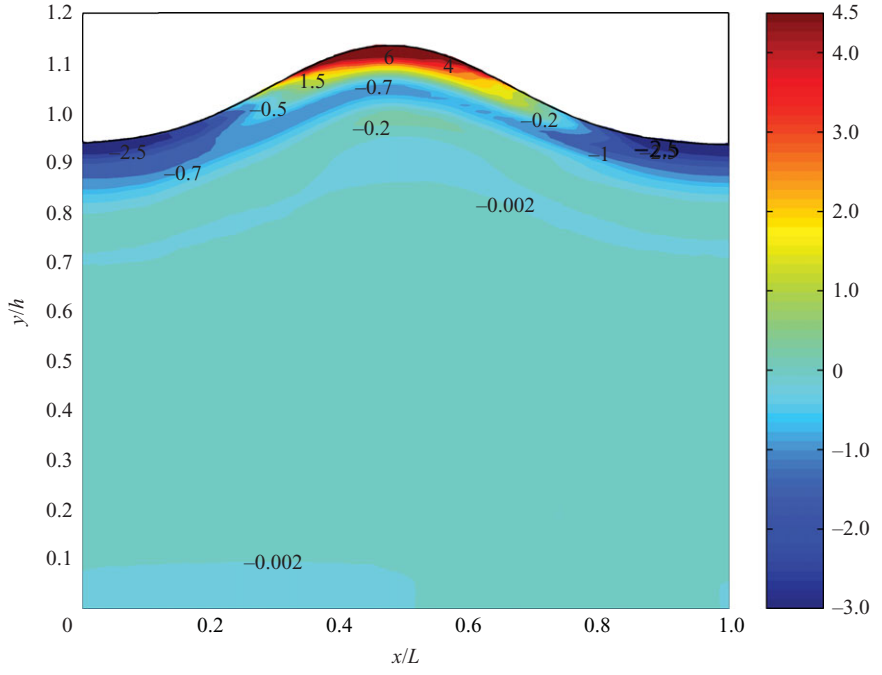

FIGURE 20. Non-dimensional vorticity ($\overline{\omega}$) in a typical wave of case C1: $2a/L = 0.04$, $h/L = 0.2$.

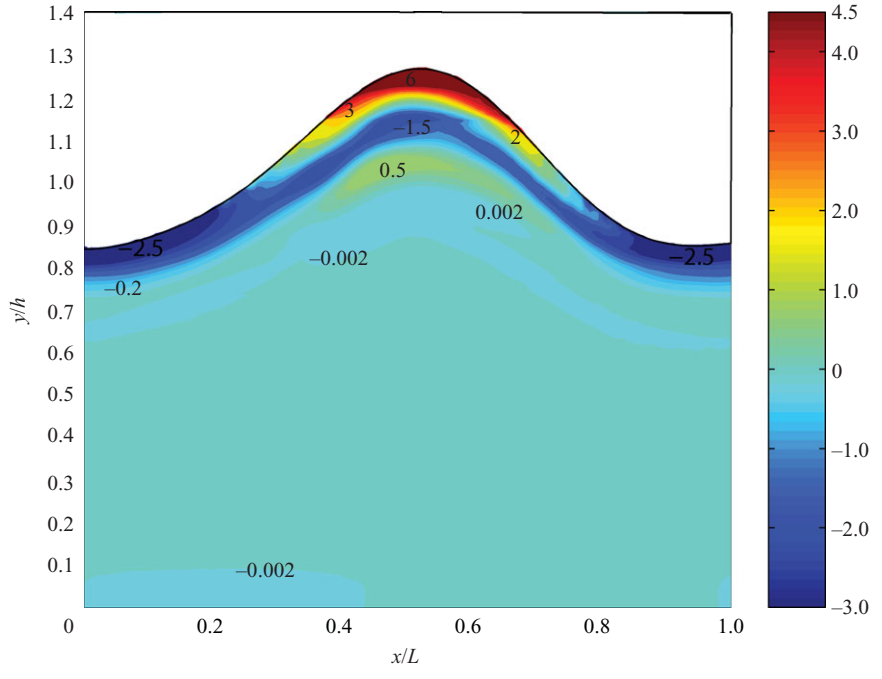

FIGURE 21. Non-dimensional vorticity ($\overline{\omega}$) in a typical wave of case C5: $2a/L = 0.08$, $h/L = 0.2$.

numerically revealed variation of vorticity on the water surface is consistent with that described by the term $-\cos(kx)$ in (4.17) and $-\cos(ks)$ given by Longuet-Higgins (1992). Under the positive vorticity region at the crest is a layer of negative vorticity which extends from trough to trough and from this layer down to the bed we observe that the layers with positive and negative vorticity reduce to smaller values with increasing in water depth.

In the cases of deep water waves as seen in figures 18 and 19, we observe that the values of non-dimensional vorticity are almost the same, this indicates that the vorticity ω is mainly proportional to $ak\sigma$; however, small differences do exist when the wave steepness changes. The vorticity layers are thinner for smaller ak in case C2 compared with case C6; larger negative vorticity magnitude in the trough region and larger positive vorticity magnitude are observed with the increase in wave steepness. Moreover, the negative vorticity layer extending from trough to trough increases in both magnitude and thickness with increase in wave steepness. Near to the bottom the vorticity magnitude is too small to be visible.

In the cases C1 and C5, referring to intermediate depth water waves as seen in figures 19 and 21, respectively, the vorticity contours show a distribution similar to the deep water depth waves, but for the same wave steepness the vorticity of intermediate depth water waves has larger magnitude due to effect of the bed, therefore for the intermediate depth water waves the bottom boundary is found to have much bigger effect on generation and diffusion of vorticity both near the free surface as well as inside the domain. On comparing the maximum vorticity magnitude in intermediate depth water waves with deep water waves, we observe an increase of 33 % and 66 % of vorticity magnitude in the crest and trough region respectively while, near the bottom boundary too, the intermediate depth water waves have larger vorticity magnitude compared with deep water waves. Thus stronger vorticity oscillations are produced with increase in wave amplitude or decrease in water depth.

To further investigate the behaviour of vorticity along the depth, the non-dimensional vorticity versus non-dimensional height is plotted at three different locations ($x/L = 0$, 0.25, 0.5) and compared with the analytical solutions given by Lamb (1932) for the Gerstner's trochoidal waves (Gerstner 1802) and for the low-Reynolds-number flow outlined by Kinsman (1965). Because of the remarkable similarity in vorticity behaviour with the depth, we present the vorticity distributions of water waves with steepness values 0.04 at these three locations in figures 22–24. The analytical solutions are plotted at locations $x/L = 0$ and 0.5 as they are the main region of interest. From figures 22–24 we can observe a remarkable similarity in vorticity behaviour with the depth at various locations. The magnitude of vorticity and the thickness of vorticity layer predicted by the numerical solutions of the viscous flow are much larger than the analytical solutions. The solution for the low Reynolds number flow suggests a very thin layer of vorticity just below the water surface and the vorticity generated on the water surface quickly reduces to zero. This is because a low Reynolds number flow is a very viscous flow, the viscosity not only prevents the production of large vorticity but also slows down the rotation of the flow very rapidly in a very thin layer. On the other hand, the solution for the Gerstner's wave is damped less quickly with depth but without oscillations.

Figure 22 depicts the vorticity magnitude varying with depth under the trough of the wave at $x/L = 0$. On comparing with analytical vorticity magnitude we observe much higher 'clockwise' rotating vortices of viscous flow. A small increase of magnitude in the deep water is observed when the wave steepness increases. For the same wave

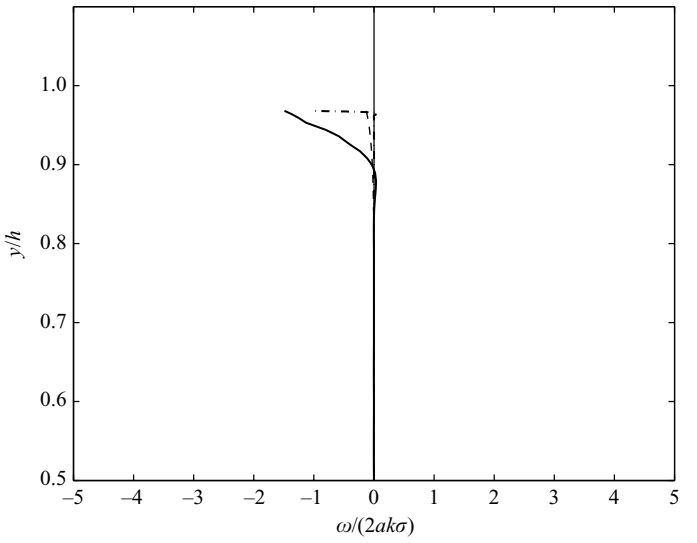

FIGURE 22. In case C2: $2a/L = 0.04$, $h/L = 0.6$: $x/L = 0$; —, the current numerical simulation result; - - -, the analytical solution for Gerstner's wave (Lamb 1932); — · —·, the analytical solution of low-Reynolds-number flow (Kinsman 1965).

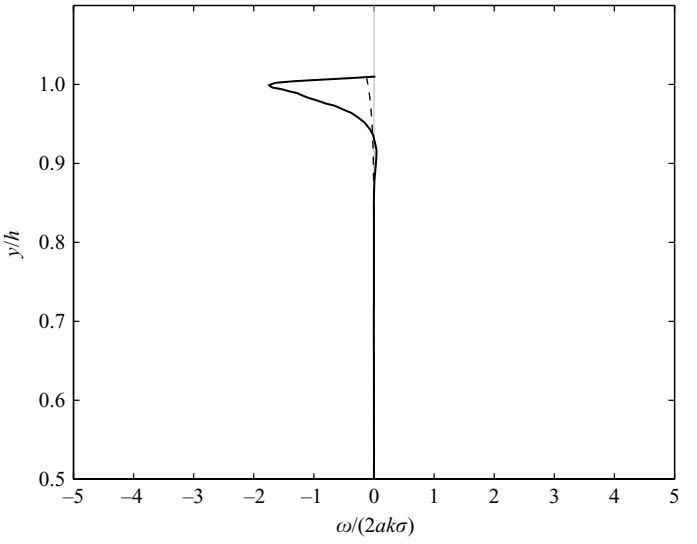

FIGURE 23. In case C2: $2a/L = 0.04$, $h/L = 0.6$: $x/L = 0.25$; —, the current numerical simulation result; - - -, the analytical solution for Gerstner's wave (Lamb 1932).

steepness we observe higher vorticity magnitude near the trough for the intermediate depth water wave in case C5 in figure 21 as compared with deep water waves from case C6 in figure 19, this is due to the bottom boundary where the velocity is zero and being nearer to both trough and crest it leads to higher velocity gradients and consequently higher vorticity.

Moving further downstream to $x/L = 0.25$, we observe, from figure 23 that the magnitude of the vorticity on the free surfaces is close to zero, but oscillatory behaviour is still produced inside the water by viscous flow. It is shown in figures 18

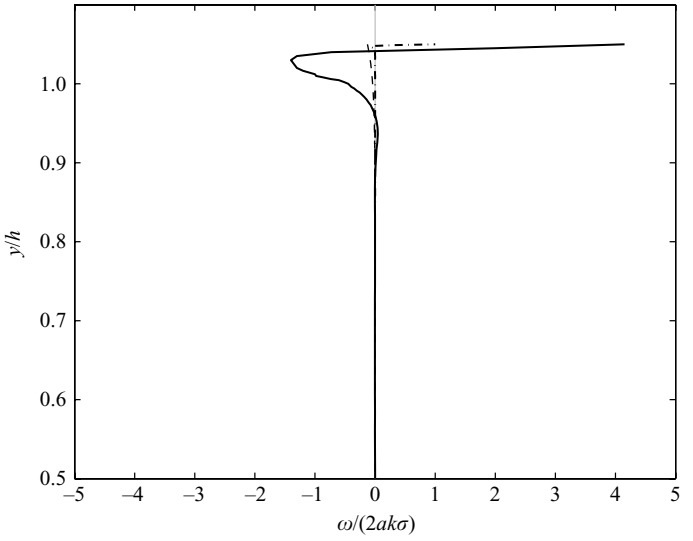

FIGURE 24. In case C2: $2a/L = 0.04$, $h/L = 0.6$: $x/L = 0.5$; —, the current numerical simulation result; - - -, the analytical solution for Gerstner's wave (Lamb, 1932); — · —·, the analytical solution of low-Reynolds-number flow (Kinsman, 1965).

and 19 that with the increase in the wave steepness from 0.04 to 0.08 in the deep water the negative vorticity layer becomes thicker. When the water depth decreases from deep water in figure 19 to the intermediate depth water in figure 21 the negative vorticity layer also becomes thicker.

As we move towards the crest at $x/L = 0.5$, in figure 24 we observe an 'anticlockwise' rotation of water flow attributed to the positive vorticity near the crest and the maximum value of positive vorticity is observed on the free surface at the crest; moreover, the maximum positive value is much higher than the maximum negative value at $x/L = 0$ and $x/L = 0.5$, and again much larger vorticity magnitude and thickness is observed than that predicted by the theories. For a small wave steepness in figure 18 the positive vorticity region is thinner than the larger wave steepness in figure 19. When water depth decreases from deep water in figure 19 to intermediate depth water in figure 21 where the wave is about to break, we observe significant increases in both negative and positive vorticities. Thus, with the decrease in depth of water, we find an increasing effect of bed on the near surface vorticity.

Moving down to the lee side of the wave at $x/L = 0.75$, the vorticity distributions are nearly repeated in magnitude and rotation along the depth and similar to location $x/L = 0.25$. Similarly, as we move towards the end of the wave at $x/L = 1$, we observe the vorticity pattern being repeated in magnitude and rotation similar to that at $x/L = 0$.

4.5. *Shear stress*

Non-dimensionalized shear stress in the flow $\overline{\tau}$ is defined by

$$\overline{\tau} = \tau_m/(2\mu_w ak\sigma), \tag{4.22}$$

where

$$\tau_m = \mu_m \left(\frac{\partial u}{\partial y} + \frac{\partial v}{\partial x} \right). \tag{4.23}$$

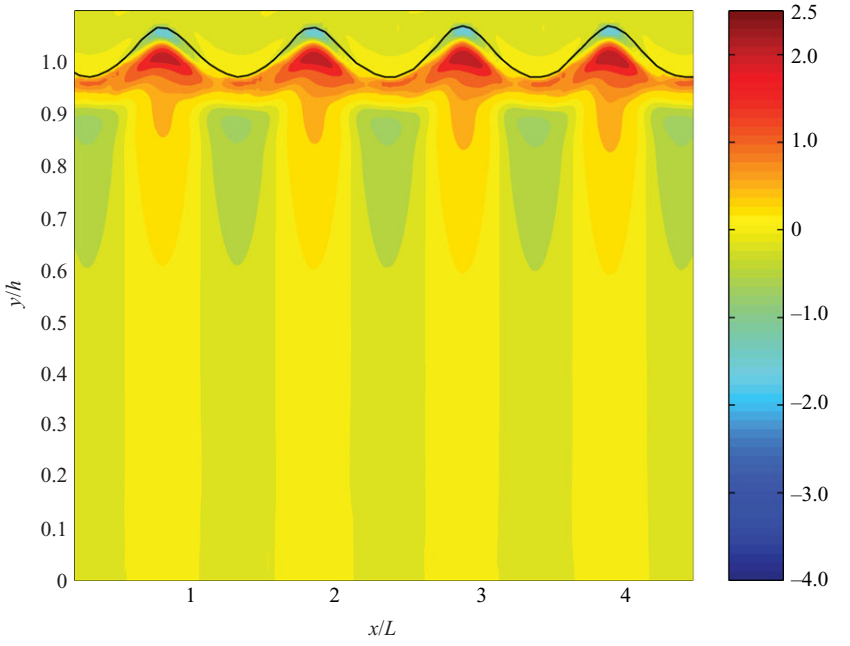

FIGURE 25. Non-dimensional shear stress ($\overline{\tau}$) contours of case C4: $2a/L = 0.06$, $h/L = 0.6$.

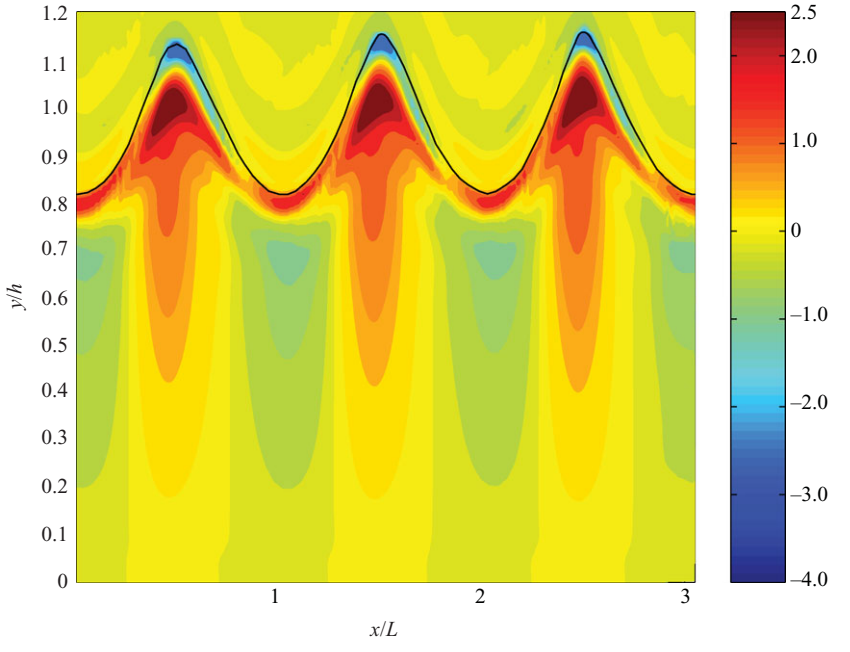

FIGURE 26. Non-dimensional shear stress ($\overline{\tau}$) contours of case C3: $2a/L = 0.06$, $h/L = 0.2$.

The distributions of non-dimensionalized shear stress in the domain for a deep water wave and a intermediate deep water are shown in figures 25 and 26 respectively. The shear stress in the air regions above the free surface shows much less variation in both cases and is much smaller compared to the water, hence aiding the assumption about

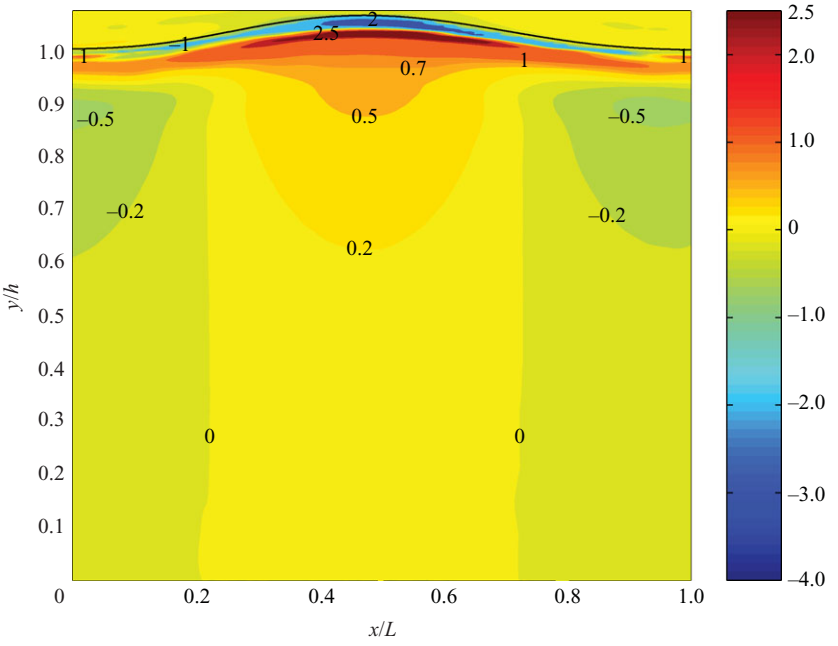

FIGURE 27. Non-dimensional shear stress ($\overline{\tau}$) contours in a typical wave in case C2: $2a/L = 0.04$, $h/L = 0.6$.

the magnitude of shear stress being considered to be zero on the free surface in the majority of the theoretical studies. However, it should be noticed that the reason of such smaller shear stress in the air is because the viscosity of air is less than 2 % of the viscosity of water, it is that this much smaller viscosity of air leads to a much smaller shear stress but the strain rate is not small near the free surface (a further discussion on the strain rate near the free surface will be given in other paper). We observe that in both cases the shear stress distributions show high degree of similarity. The most important feature is the existence of a periodic thick layer of shear stress under the water surface. From the free surface to inside of the water, shear stress increases rapidly under the crest and trough. We observe in both cases that a maximum shear stress which is positive is inside the water but close to the free surface of the crest. A negative shear stress layer is observed near the crest and under this layer there is a positive shear layer extending from trough to trough. Under the crest, this positive shear stress layer extends down to the bottom and under the trough the positive shear stress layer oscillates to a negative shear stress region which extends to the bottom and the magnitude of shear stress becomes smaller with the increase in the depth. Under the large shear stress layer near the free surface, most of the domain of water wave is divided into vertical stripes by vertical lines on which the shear stress is zero and in the stripes under the crest the shear stress is positive while under the trough it is negative.

We analyse a typical wave in all the cases by a detailed observation. In the deep water wave cases C2 and C6 as seen in figures 27 and 28 we observe that with the increase of the wave steepness the area of negative shear stress the crest extends less horizontally but becomes thicker in vertical direction. We also observe that the contour lines move downwards when the wave steepness increase, this indicates that shear stress in whole solution domain increases with the increase of the wave

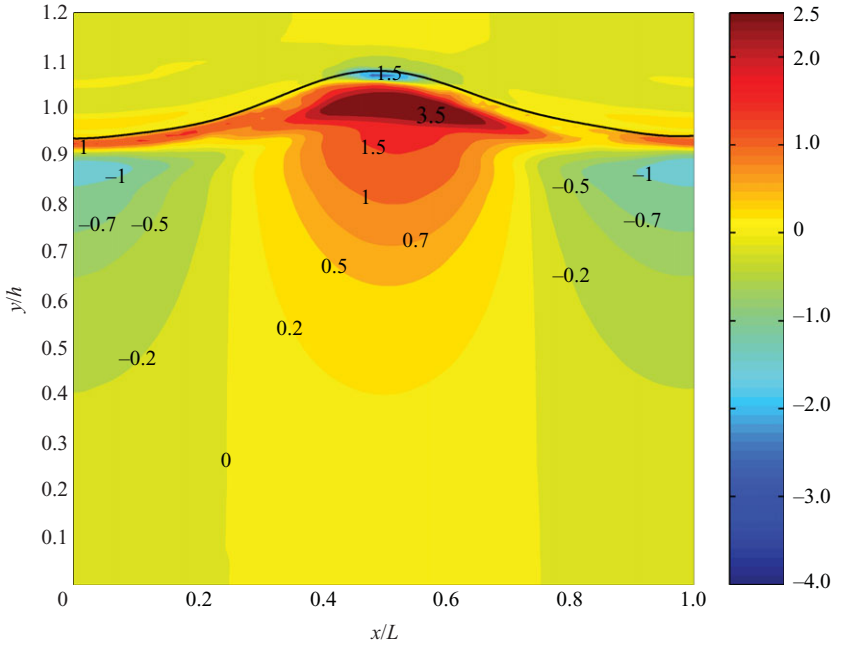

FIGURE 28. Non-dimensional shear stress ($\overline{\tau}$) contours in a typical wave in case C6: $2a/L = 0.08$, $h/L = 0.6$.

steepness. Similar to the deep water waves, the shear stress in the intermediate depth water waves in figures 29 and 30 increases when the wave steepness increases and a larger increase takes places under the crest and trough. A significant increase in positive shear stress occurs under the crest in figure 30 where the wave is about to break. On comparing the intermediate depth water waves with deep water waves, we observe that intermediate depth waves produce larger magnitude shear stresses in whole solution domain, this is clearly caused by the effect of bottom, which is due to the increase in vertical velocity gradient inside the water because the bottom boundary restricts the movement of water particles along the desired path. Therefore, the bed has larger effect on the flow in the intermediate depth water.

5. Conclusion

A numerical scheme developed by Zwart, Burns & Galpin (2007) that uses the VOF for interface tracking has been successfully applied to the numerical simulation of two dimensional progressive and viscous water waves. A second-order implicit time stepping scheme, the second-order upwind biased scheme for momentum conservation and high resolution scheme for mass conservation are found to be efficient for solving full Navier–Stokes equations for the nonlinear, transient and viscous water waves. The numerical results for decay of energy are in excellent agreement with the theoretical and experimental results of Mitsuyasu & Honda (1982). Other interesting aspects in water waves such as velocity vectors and streamlines have been compared with their counterpart given by the potential flow. The numerical solutions have also revealed the effect of nonlinearity on the profiles of free surface. We have found that the potential flow is inaccurate for describing many aspects of energy dissipation, vorticity and shear stress of real water waves. An objective analysis on the effect of

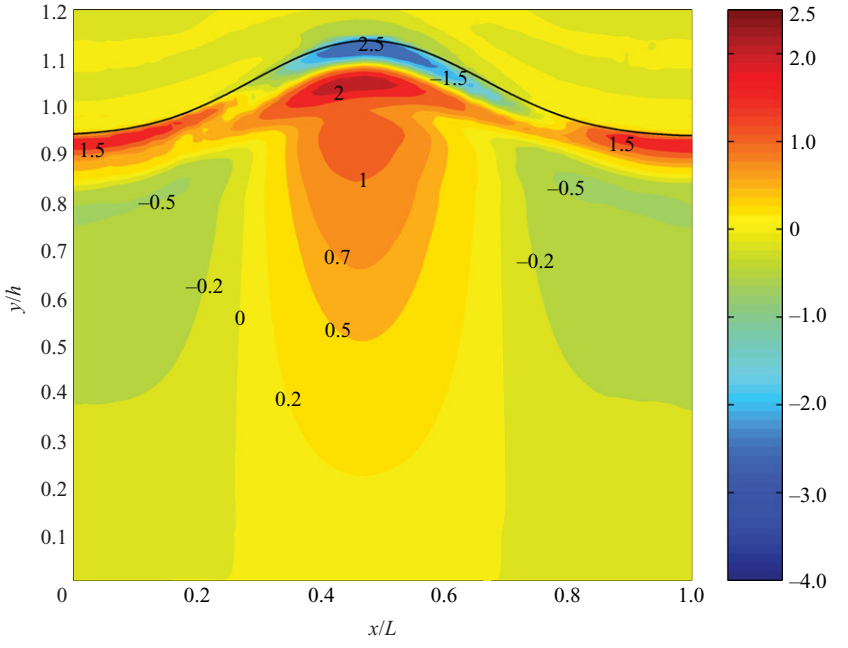

FIGURE 29. Non-dimensional shear stress ($\overline{\tau}$) contours in a typical wave in case C1: $2a/L = 0.04$, $h/L = 0.2$.

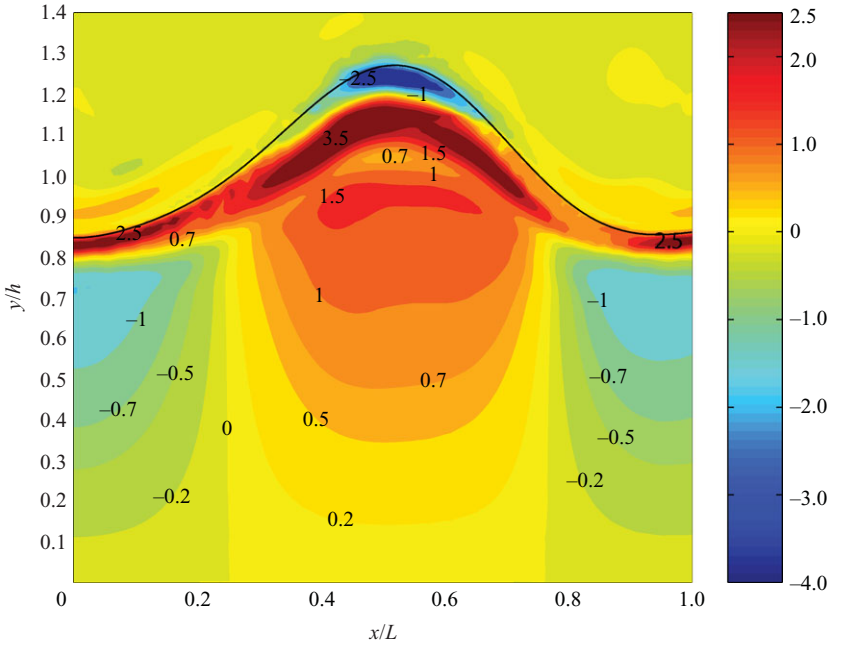

FIGURE 30. Non-dimensional shear stress ($\overline{\tau}$) contours in a typical wave in case C5: $2a/L = 0.08$, $h/L = 0.2$.

viscosity on the water waves has been carried out and revealed interesting features of the vorticity and shear stress in the water waves. The numerical results of vorticity show 'clockwise' and 'anticlockwise' vortices in the whole domain of water waves, signifying oscillatory behaviour of vorticity. Similarly, oscillations of shear layers are also observed on the crest and trough of the water wave and maximum shear stress is inside the crest of water wave, just below the free surface. The numerical results also show that the wave steepness and water depth significantly affect the water waves. The effects of shear stress inside the water waves have received less attention but are here shown to be an important aspect in water waves. It can be expected that the viscous effects play a larger role when studying mass and momentum transfer in the coupled air–sea interaction.

We thank Dorothy Hodgkin Postgraduate Awards under UK Government for funding the study of Ashish Raval. We thank Natural Environmental Research Council (NERC) and British Petroleum (BP) who kindly sponsored the funding for the awards. We also sincerely thank the referees for their constructive comments.

REFERENCES

Barth, T. J. & Jesperson, D. C. 1989 The design and application of upwind schemes on unstructured meshes. *AIAA Paper 89–0366.*

Behroozi, F. 2004 Fluid viscosity and the attenuation of surface waves: a derivation based on conservation of energy. *Eur. J. Phys.* **25**, 115–122.

Chen, C. J. & Chen, H. C. 1982 The finite-analytic method. *Tech. Rep.* IIHR Rep. 232-IV, Iowa Institute of Hydraulic Research, University of Iowa.

Chen, C. J. & Chen, H. C. 1984 Finite analytical numerical method for unsteady two-dimensional Navier–Stokes equations. *J. Comput. Phys.* **53**, 209–222.

Chen, B. F. & Nokes, R. 2005 Time-independent finite difference analysis of fully non-linear and viscous fluid sloshing in a rectangular tank. *J. Comput. Phys.* **209**, 47–81.

Cheung, T. K. & Street, R. L. 1988 Turbulence layers in the water at an air–water interface. Part A. *J. Fluid Mech.* **194**, 133–151.

Constantin, A. 2001 On the deep water wave motion. *J. Phys.* A*: Math. Gen.* **194**, 1405–1417.

Constantin, A., Sattinger, D. & Strauss, W. 2006 Variational formulations for steady water waves with vorticity. *J. Fluid Mech.* **548**, 151–163.

Corte, C. & Grilli, S. T. 2006 Numerical modelling of extreme wave slamming on cylindrical offshore support structures. In *Proceedings of the Sixteenth International Offshore and Polar Engineering Conference*, San Francisco, CA.

Dabiri, D. & Gharib, M. 1997 Experimental investigation of the vorticity generation within a spilling water wave. *J. Fluid Mech.* **330**, 113–139.

Dalrymple, R. A. & Kirby, T. J. 1986 Water waves over ripples. *J. Waterway Port Coast. Ocean Engng* **112**, 309–319.

Dalrymple, R. A. & Rogers, B. D. 2005 Numerical modeling of water waves with the SPH method. *J. Coast. Engng* **53**, 141–147.

Darwish, M. S. & Moukalled, F. 2003 TVD Schemes for unstructured grids. *Intl J. Heat Mass Transfer* **46**, 599–611.

Dean, R. G. & Dalrymple, R. A. 1984 *Water Wave Mechanics for Engineers and Scientists.* Prentice-Hall.

Dong, C. M. & Huang, C. J. 2004 Generation and propagation of water waves in a two-dimensional numerical viscous wave flume. *J. Waterway Port Coast. Ocean Engng* ASCE **130** (3), 143–153.

Drew, D. A. & Passman, S. L. 1999 *Theory of Multicomponent Fluids.* Springer.

Duncan, J. H., Philomin, V., Behres, M. & Kimmel, J. 1994 The formation of spilling breaking water waves. *Phys. Fluids* **6**, 2558–2560.

Dutykh, D. & Dias, F. 2007 Viscous potential free-surface flows in a fluid layer of finite depth. *C. R. Acad. Sci. Paris Ser.* I **345**, 113–118.

Fulgosi, M., Lakehal, D., Banerjee, S. & De Angelis, V. 2003 Direct numerical simulation of turbulence in a sheared air–water flow with a deformable interface. *J. Fluid Mech.* **482**, 319–345.

Gerstner, F. J. 1802 Theorie der Wellen, Abh. d. k. bhom. Ges. D. Wiss. Reprinted in Ann. der Physik 1809 **32**, 412–440.

Harlow, F. H. & Welch, J. E. 1965 Numerical calculation of time-dependent viscous incompressible flow of fluid with free surface. *Phys. Fluids* **8**, 2182–2189.

Hirt, C. W. & Nichols, B. D. 1981 Volume of fluid (VOF) method for the dynamics of free boundaries. *J. Comput. Phys.* **39**, 201–225.

Hou, T. Y., Lowengrub, J. S. & Shelley, M. J. 2001 Boundary integral methods for multicomponent fluids and multiphase materials. *J. Comput. Phys.* **169**, 302–323.

Huang, C. J., Zhang, E. C. & Lee, J. F. 1988 Numerical simulation of nonlinear viscous wavefelds generated by a piston-type wavemaker. *J. Engng Mech.* ASCE **123** (10), 1110–1120.

Hur, D. S. & Mizutani, N. 2003 Numerical estimation of the wave forces acting on a three-dimensional body on submerged breakwater. *Coast. Engng* **47**, 329–345.

Hutchinson, B. R. & Raithby, G. D. 1986 A multigrid method based on the additive correction strategy. *Numer. Heat Transfer* **9**, 511–537.

Jacqmin, D. 1999 Calculation of two-phase Navier–Stokes flows using phase-field modeling. *J. Comput. Phys.* **155**, 96–127.

Jamet, D., Lebaigue, O., Coutris, N. & Delhaye, J. M. 2001 The second gradient method for the direct numerical simulation of liquid–vapor flows with phase change. *J. Comput. Phys.* **169**, 624–651.

Kleinstreuer, C. 2003 *Two-Phase Flow, Theory and Applications*. Taylor & Francis.

Kinsman, B. 1965 *Wind Waves: Their Generation and Propagation on the Ocean Surface*. Prentice Hall.

Lamb, H. 1932 *Hydrodynamics*. Cambridge University Press.

Li, B. & Fleming, C. A. 2001 Three-dimensional model of Navier–Stokes equations for water waves. *J. Waterway Port Coast. Ocean Engng* **127**, 16–25.

Lin, P. 2008 *Numerical Modeling of Water Waves*. Taylor & Francis.

Lin, J. C. & Rockwell, D. 1995 Evolution of a quasi-steady breaking wave. *J. Fluid Mech.* **302**, 29–44.

Liu, P. L.-F. & Lin, P. 1997 A numerical model for breaking waves: the volume of fluid method. *Tech. Rep.* CACR-97-02. Centre for Applied Coastal Research, University of Delaware.

Liu, P. L.-F. & Orfila, A. 2004 Viscous effects on transient long-wave propagation. *J. Fluid Mech.* **520**, 83–92.

Longuet-Higgins, M. S. 1992 Capillary rollers and bores. *J. Fluid Mech.* **240**, 659–679.

Lundgren, T. & Koumoutsakos, P. 1999 On the generation of vorticity at a free surface. *J. Fluid Mech.* **382**, 351–366.

Maronnier, V., Picasso, M. & Rappaz, J. 2003 Numerical simulation of three-dimensional free surface flows. *Intl J. Numer. Methods Fluids* **42**, 697–716.

Milne-Thomson, L. M. 1994 *Theoretical Hydrodynamics*. Dover.

Mitsuyasu, H. & Honda, T. 1982 Wind-induced growth of water waves. *J. Fluid Mech.* **123**, 425–442.

Monaghan, J. J. 1994 Simulating free surface flows with SPH. *J. Comput. Phys.* **110**, 399–406.

Monaghan, J. J. & Kos, A. 1999 Solitary waves on a Cretan beach. *J. Waterway Port Coast. Ocean Engng* **125** (3), 145–154.

Park, J. C., Kim, M. H., Miyata, H. & Chun, H. H 2003 Fully nonlinear numerical wave tank (NWT) simulation and wave run-up prediction around 3-D structures. *Ocean Engng* **30**, 1969–1996.

Peirson, W. L, Garcia, A. W. & Pells, S. E. 2003 Water wave attenuation due to opposing wind. *J. Fluid Mech.* **487**, 345–365.

Raw, M. 1996 Robustness of coupled algebraic multigrid for the Navier–Stokes equations. *AIAA Paper 96-0297*.

Rhie, C. M. & Chow, W. L. 1983 Numerical study of the turbulent flow past an airfoil with trailing edge separation. *AIAA J.* **21**, 1525–1532.

Saffman, P. G. 1981 Dynamics of vorticity. *J. Fluid Mech.* **106**, 49–58.

Scardovelli, R. & Zaleski, S. 1999 Direct Numerical Simulation of free-surface and interfacial flow. *Annu. Rev. Fluid Mech.* **31**, 567–603.

Schneider, G. E. & Raw, M. J. 1987 Control volume finite-element method for heat transfer and fluid flow using collocated variables −1. Computational procedure. *Numer. Heat Transfer* **26**, 367–380.

Sethian, J. A. 1999 *Level Set Methods and Fast Marching Methods: Evolving Interfaces in Computational Geometry, Fluid Mechanics, Computer Vision, and Materials Science*. Cambridge University Press.

Teles Da Silva, A. F. & Peregrine, D. H. 1988 Steep, steady surface waves on water of finite depth with constant vorticity. *J. Fluid Mech.* **195**, 281–302.

Thais, L. & Magnaudet, J. 1995 A triple decomposition of the fluctuation motion below laboratory wind water waves. *J. Geophys. Res.* **100**, 741–755.

Thomas, T. G., Leslie, D. C. & Williams, J. J. R. 1995 Free surface simulations using a conservative 3D code. *J. Comput. Phys.* **116**, 52–68.

Tryggvason, G., Bunner, B., Esmaeeli, A., Juric, D., Al-Rawahi, N., Tauber, W., Han, J., Nas, S. & Jan, Y. J. 2001 A front-tracking method for the computations of multiphase flow. *J. Comput. Phys.* **169**, 708–759.

Tsai, W. T. & Yue, D. K. P. 1996, Computation of nonlinear free-surface flows. *Annu. Rev. Fluid Mech.* **28**, 249–278.

Vanden-Broeck, J. M. 1996 Periodic waves with constant vorticity in water of infinite depth. *IMA J. Appl. Math.* **56**, 207–217.

Wang, J. & Joseph, D. D. 2006 Purely irrotational theories of the effect of the viscosity on the decay of free gravity waves. *J. Fluid Mech.* **559**, 461–472.

Zwart, J. P. 2005 Numerical Modelling of free surface and cavitating flows. In *VKI Lecture Series: Industrial Two-Phase Flow CFD*. von-Karman Institute lecture series 2004-2005; 2004. p. 25.

Zwart, J. P., Burns, D. A. & Galpin, F. P. 2007 Coupled algebraic multigrid for free surface flow simulations. In *Proceedings of Twenty-Sixth Intl Conf. on Offshore Mechanics & Arctic Engineering*, OMAE 2007-29080, San Diego, USA.

Zwart, J. P., Scheuerer, M. & Bogner, M. 2003 Free surface modelling of an impinging jet. In *ASTAR International Workshop on Advanced Numerical Methods for Multidimentional Simulation of Two-Phase Flow*, Garching, Germany.